Dual-band absorber for multispectral plasmon-enhanced infrared photodetection

Peng Yu[a*], Jiang Wu[b], Eric Ashalley[a], Alexander Govorov[c], Zhiming Wang[a*]

[a]*Institute of Fundamental and Frontier Science, University of Electronic Science and Technology of China, Chengdu 610054, P. R. China.*

[b]*Department of Electronic and Electrical Engineering, University College London, Torrington Place, London WC1E 7JE, United Kingdom.*

[c]*Department of Physics and Astronomy, Ohio University, Athens, OH 45701, USA*

**Corresponding author: Azarisyu@gmail.com; zhmwang@uestc.edu.cn*

ABSTRACT

For most of the reported metamaterial absorbers, the peak absorption only occurs at one single wavelength. Here, we investigated a dual-band absorber which is based on simple gold nano-rings. Two absorption peaks can be readily achieved in 3-5 μm and 8-14 μm via tuning the width and radius of gold nano-rings and dielectric constant. The average maximum absorption of two bands can be as high as 95.1% (-0.22 dB). Based on the simulation results, the perfect absorber with nano-rings demonstrates great flexibility to create dual-band or triple-band absorption, and thus holds potential for further applications in thermophotovoltaics, multicolor infrared focal plane arrays, optical filters, and biological sensing applications.

Keywords: Metamaterials, Dual-band, Plasmonics, Infrared detector, Perfect absorber, FDTD.

1. Introduction

Artificial metamaterials (MMs) are widely studied for their exotic properties i.e. negative refractive index [1], and potential device-applications such as perfect lenses[2] and invisibility cloaks[3,4]. Composite optical MMs are innovative structures for customizing electric and magnetic properties for specific applications, which are based on fundamental resonance of the resonators. For the last ten years, researchers have presented MMs with the state-of-the-art performances from radio[5,6], microwave[7,8], mm-Wave[9-11], THz[12,9,13], FIR[14], MIR[15-17], NIR[18,19], to optical spectrum[20,21]. Specifically, metamaterial perfect absorber (MMPA), first demonstrated by Landy *et al.*[22], shows the merits of MMs such as highly absorptive characteristics, tunable resonant frequencies, and undemanding manufacturability for a high Q-factor. Intrigued by MMPA and possibility for near unity absorbance, MMPAs have become attractive for various optoelectronic applications, including detectors[23,24], emitters[25], imaging devices[26], solar cells[27], etc.

Extensive efforts have been made to harness energy harvesting applications. For infrared (IR) detector application, to provide perfect signal-to-noise performance and an extremely fast response, traditional methods and materials require cryogenic cooling, sacrificing their convenience and scalability and makes them bulky, heavy, pricy. The IV-VI materials demonstrate available low gap and were fully studied, but with poor mechanical property and large permittivity. The III-V materials has matured dopants and fabrication technology and possible monolithic integration, but they demonstrate heteroepitaxy with large lattice mismatch. Recently, quantum dot and quantum well were used in the photodetection [28]. However, the weak absorption of quantum dots / well, challenge in achieving a uniform quantum structure size and low operating temperatures have not been addressed yet. Selective emitters using luminescent bands of rare earth oxides are limited in scarcity of materials and complication of controlling compounds [29,30]. Additionally, nonresonant nature of photonic crystal emitters impose restrictions on boosting efficiencies [31].

The MMPAs with hundreds of nanometers present perfect absorption at specific wavelengths, consuming less material and lessening fabricate process. The pivotal focus for MMPA design is to minimize reflection and transmission while balancing electric and magnetic resonances to maximize absorption. Although rapid progress has been made in terahertz frequency domain [32-36], most MMPA designs are single-band at specific frequency with limited applications. Compared with the single-band absorbers, the dual-band devices have many advantages such as better image contrast, longer detecting distance and higher spatial resolution at targeted wavelengths. However, traditional dual-band detectors have low signal response with low responsivity and poor detection characteristics because of their multi-surface and complex components of materials. Recently, researchers have demonstrated multiband MMPAs with two or more well-defined absorption peaks [37-42]. For instance, triple-band polarization-independent metamaterial absorber are reported for GHz absorption based on millimeter-sized square strips [42]. The general structure is comprised of a highly conductive and geometrically shaped metallic resonator, i.e. gold and copper, and metal-dielectric layers with various arrangements, which oscillate electrons in a unit cell. Physically, engineered impedance matching $Z_{eff} = (\mu_{eff}/\varepsilon_{eff})^{1/2}$, complex electric permittivity and complex magnetic permittivity need to be taken into account. If the $Z_{eff} = 1$, then the bulk effective impedance of MMs matches the Z_{eff} of free space medium such as air and vacuum. By tuning ε and μ simultaneously, the reflectance weakens approximately to zero; indicating full light absorption and thus no penetrating radiation and no reflection.

Here we present a design of MMPA with a double-ring geometry that is insensitive to the polarization of light. Here we used a single unit cell in the propagation direction achieving two maximum absorptions

as high as average 95.1% (-0.22 dB) with a much smaller thickness than the resonant wavelengths. The scalability with wavelengths permits applications for bolometric pixel elements and pyroelectric detectors. Our design can be especially useful for bolometers with a narrow band response; such bolometers are used as focal plane array (FPA) detectors for imaging. Meanwhile, the proposed detector also has potential use for combustible, toxic and harmful gases, such as CH_4, CO, C_2H_6 in MIR region, SO_2F_2 and SF_6 in FIR, thermographic cameras, hyperspectral imaging, meteorology, free space light communication, remote sensing, laser, and identification biological compounds, etc.

2. Simulation methodology

Fig. 1 shows MMPA structures proposed in this study, demonstrating the 3D construction of the structure which includes a thick Si substrate at the bottom, a layer of gold thin film with fixed thickness, a dielectric spacer layer and a gold nanoresonator at the top respectively. In this structure, the thickness of gold film is much larger than typical skin depth so that the $A(\omega)$ can be simplified as 1 - $R(\omega)$, where $A(\omega)$ and $R(\omega)$ are absorptivity and reflectance respectively. Fig. 1b demonstrates the top view of the surface which is incorporated with a nano-ring as a coupler to trap light in. The ring is 100 nm thick and capable of altering by tuning parameters of *R* and *r*, while the lattice constant is defined as *P*. The performance of this single-band MMPA extremely counts on these variates.

Enlightened by the single band absorber, we designed the dual-band MMPA based on two concentric rings. Fig. 1c exhibits the dual-band MMPA including almost identical structure with the single-band structure. The only distinction is the addition of another concentric ring; the separation distance between two rings is defined as *S*. While the absorption of the device is relevant with geometrical parameters in single-band, the dual-band MMPA can also be engineered through the *S*, component also crucial for non-loss absorption at specific frequencies, as illustrated in Fig. 1d.

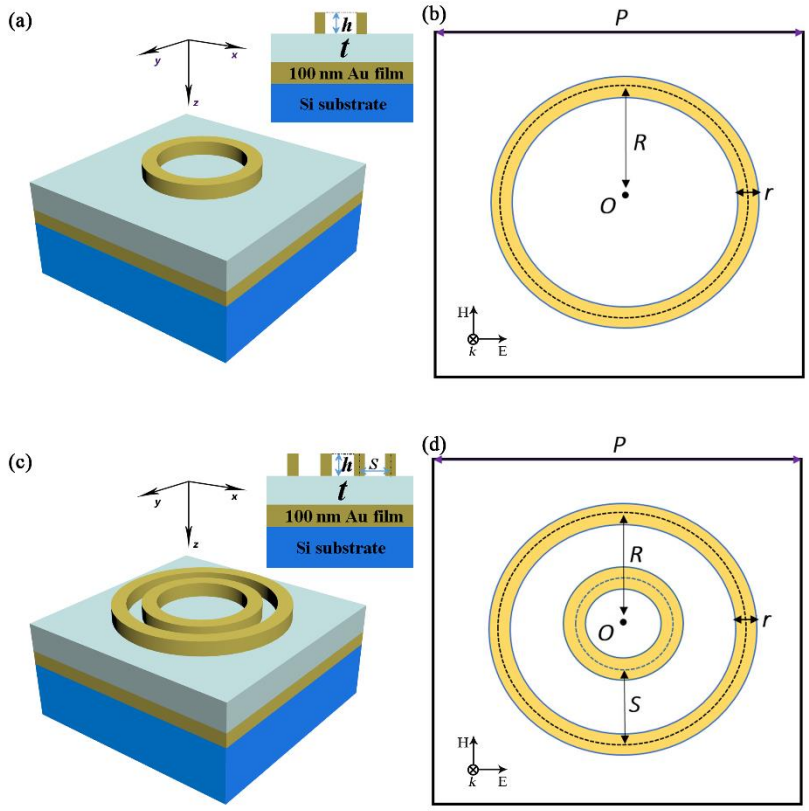

Fig. 1 Schematic illustration of a periodic single-band MMPA. **a** Side view of the

structure with a gold-ring of the height h = 100 nm, dielectric spacer with a thickness t, 100 nm gold film and silicon substrate. **b** Top view of the ring resonator with a width r, lattice constant P and radius R. **c** Side view of the structure incorporating paired gold concentric rings with height h = 100 nm, dielectric spacer with a thickness t, 100 nm gold film, distance S between two rings, and silicon substrate from top to bottom. **d** Top view of the double ring structure with the parameters: The ring widths r, lattice constant P, radius R and distance between two rings S. The surface of dielectric spacer is set as 0 in Z direction

To design such structure, the overriding criteria is to certify the availability and reliability. Finite difference time domain (FDTD) method, based on Maxwell equation for theoretical study, shows its flexibility on design, analysis and optimization for photonic devices and materials. It provides a route to reducing dependence upon costly experimental prototypes, and breeds quicker assessment of designs [43,22,44]. Here, we simulated MMPAs with gold-ring placed on the top to provide dual-band absorptions at targeted frequencies while upholding tunability and flexibility. By altering corresponding parameters, maximum absorptions at desired frequencies between 3-5 μm (middle infrared, MIR) and 8-14 (far infrared, FIR) μm can be realized. A single unit cell was simulated with appropriate boundary conditions as illustrated in Fig. 1. The wave vector $\boldsymbol{k}$ propagates through the Z direction with perfect magnetic field in y-z plane and perfect electric field in x-z plan. Perfectly matched layers (PML) was applied in the propagation direction in order to eliminate nonphysical reflections at domain boundaries and the periodic boundary condition (PBC) is adopted to simulate a structure which is periodic in one direction but not necessarily in other directions. The refractive index of materials are modelled using fitted optical data Au[45], silicon[46] and silicon dioxide[46]. Ideal dielectric spacer with different refractive indexes to replace SiO_2 is investigated. According to the proposed structure, the TEM wave is reflected and absorbed when the incident radiation is perpendicular to the surface. So, the absorption hinges on Eq. (1)

$$A(\omega) = 1 - \left|S_{21}(\omega)\right|^2 - \left|S_{11}(\omega)\right|^2 = 1 - T(\omega) - R(\omega) \quad (1)$$

where $\left|S_{11}(\omega)\right|$ and $\left|S_{21}(\omega)\right|$ are the complex reflection and transmission coefficients respectively, which determine $R(\omega)$ and $T(\omega)$. Because of the existence of semi-infinite Au film, transmission vanished in the substrate, and the equation can be simplified as $A(\omega) = 1 - R(\omega)$.

3. Results and discussion

As shown in Fig. 2, the proposed structure composing of a single ring atop exhibits narrow electromagnetic absorption peak centered at MIR and FIR region. The ring on the top creates a resonant response as a function of wavelength, while the Au film functions together with the spacer to generate strong coupling to magnetic component of the normal incident plane source. The lattice constant P has linear dependency with resonant wavelength and peaked absorption (features critical for light harvesting). As the P increases, the peak shifts to shorter wavelength, where plasmon resonances are excited. Full width at half maximum (FWHM) narrows down linearly as the P increase, giving rise to high distinguishability. While the resonant wavelengths respond sensitively to R and n with linear positive correlations, it is negligible for P and r, as indicated in Fig. 3. On the other hand, maximum absorptions are positively correlated with P, R, n and negatively correlated with ring width r. This phenomena are mainly attributed to the electromagnetic coupling efficiency. Smaller r with sharp edge have stronger

near field enhancement than the larger *r*, thus coupling more energy. Larger *P* and *R* can concentrate more energy in a unit cell and avoid out-coupling. Besides, Ohmic losses contribute partially to the non-perfect absorption.

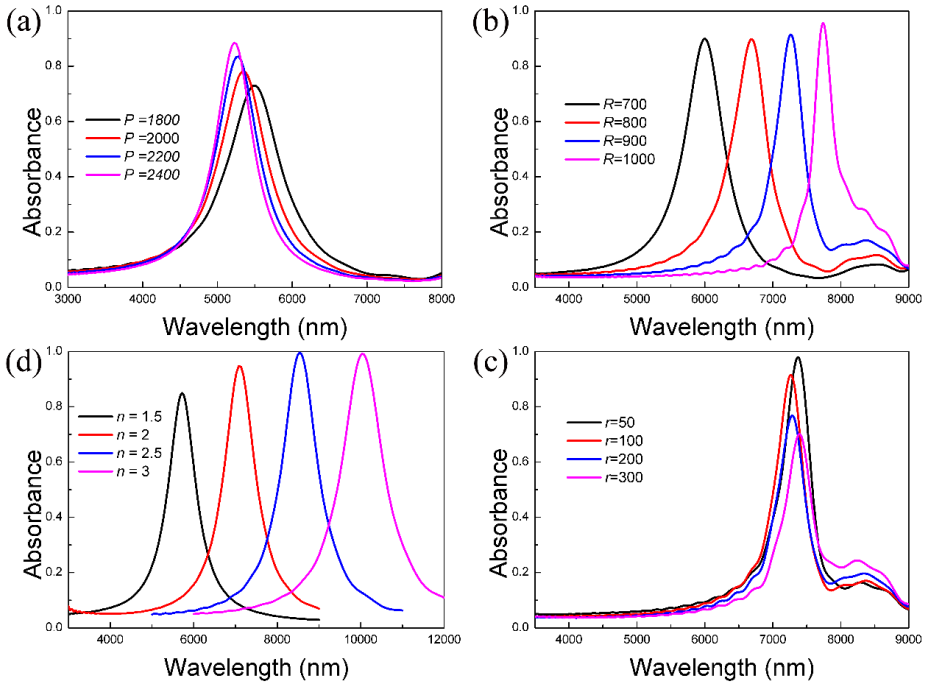

Fig. 2 Absorbance properties of single-ring MMPA with different parameters. **a** Variation of lattice constant *P*. **b** Variation of radius of ring *R*. **c** Variation of refractive index *n*. **d** Variation of ring width ***r***. The dielectric spacer is silicon dioxide

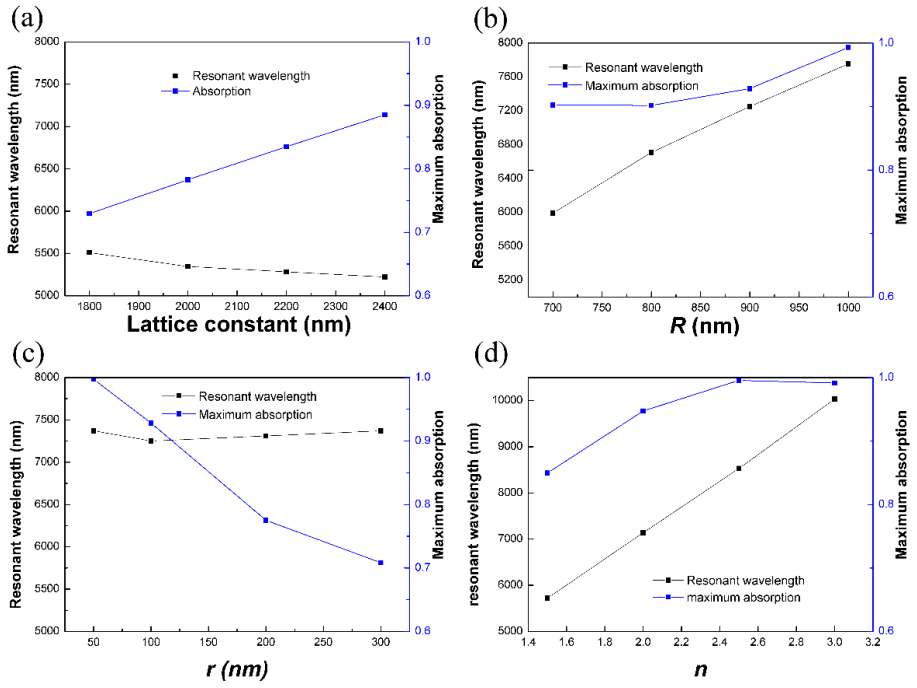

Fig. 3 Resonant wavelength and maximum absorption dependence of single-ring MMPA with different parameters, matching with Fig. 2. **a** Lattice constant *P*. **b** Radius of ring *R*. **c** Ring width ***r***. **d** Refractive index *n*. The dielectric spacer is silicon dioxide

To the end, we demonstrate a dual-band MMPA with considerable signal-to-noise ratio by using this ring-shaped resonator after investigating the properties of the single band. The data from simulations dovetail with our expectation. The two ring-shaped resonators support two resonances at targeted wavelength bands distributed in MIR and FIR respectively with different ring radii. As shown in Fig. 4, the two first-order resonant modes, M1 (short-wavelength) and M2 (long-wavelength), appear at MIR and FIR. Fig. 4a, b and c clarify the relationship between *S* and *t*. The *S* and the absorption curves are demonstrated in Fig. 4 a. It can be seen that the larger *S* pushes two bands toward MIR and FIR and the two bands have almost similar FWHM. In Fig. 4 (b), while the resonance mode M1 shifts linearly to blue, the M2 shifts to red. Dielectric spacer is also critical for optimization during design consideration because the spacer thickness controls radiation damping. As shown in Fig. 4c, for *S* = 400 nm and 600 nm, the optimum absorption can be achieved when *t* = 290 nm and deviation from this value dwarfs the peaks. Contrary to one's research with different optimum *t* for various offset [43], our result shows same optimum *t* for different *S*. Their cross-shaped structure reaches maximum absorbance at different MgF_2 thickness due to the coupling strength of two modes brought about by asymmetry. Owing to the symmetry in our simulation, this ring-shaped structure have potential on practical application with simplification. To achieve average maximum absorbance above 80%, the *t* can be tuned from 150~550 nm for *S* = 400 nm and 175~550 nm for *S* = 600, allowing deviation with fabrication flexibility. Fig. 4d demonstrates peaks in MIR and FIR with tunability at interested wavelengths. The two clearly resolved absorption peaks were selected arbitrarily within 3-5 and 8-14 μm for our proof-of-concept by modifying *R* and *n*. For ideal dielectric spacer, the resonant wavelength is only influenced by radius of ring. It is worth noting that the individual ring leads to blueshift of the resonant frequency, different from presence of two rings simultaneously. This phenomenon can be attribute to the anti-parallel surface current oscillation in the neighboring rings and can be relieved by increasing the ring distance *S*. However, modification of one ring has no effect on another resonant band for two rings structure.

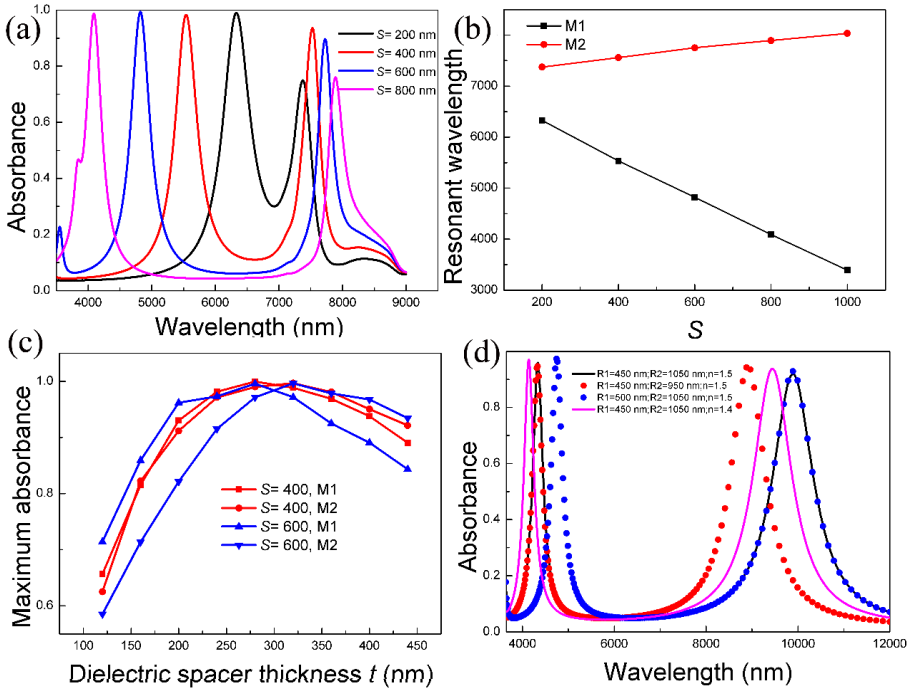

Fig. 4 Resonant wavelength and maximum absorption dependence of dual-band MMPA with *S*, *R* and *t*. **a** Absorbance spectra with increasing *S* at *t* = 280 nm. **b** Relationship between two excited modes with increasing *S* . **c** Relationship between

maximum absorbance and *t*. **d** *R* and *n* for customizing at *t* = 250 nm. For **a~c**, dielectric spacer is silicon dioxide and for **d**, the *n* of spacer is set to 1.4 and 1.5

To interpret the mechanism behind this enhancement, Fig. 5 and Fig. 6 show the spatial distribution of electric (***E***) and magnetic (***H***) fields for structure plotted in Fig. 4d (black line). The enhancement factor, $\boldsymbol{E/E_0}$ and $\boldsymbol{H/H_0}$, provides insight into the mechanism behind the enhancement where ***E*** and ***H***, $\boldsymbol{E_0}$ and $\boldsymbol{H_0}$ are the intensity of electric field and magnetic field respectively at given position and that would occur at the same position in the absence of gold ring. It can be seen from Fig. 5 and Fig. 6 that magnetic field and electric field are enhanced dramatically at resonant wavelengths 4332 nm and 9890 nm respectively. The local field intensity is even 20~140 times larger than the ring-absent structure. The electric component of the plane wave can couple the electric field strongly because two gold rings afford local surface plasmon resonances (LSPRs) and surface plasmon polaritons (SPPs). For magnetic component, it gives rise to antiparallel surface current on the rings and the ground metal plane, leading to the magnetic coupling and the response, as shown in Fig. 7. Utilizing the surface plasmon (SP) mode, various nanostructured absorbers have been achieved, such as nano-apertures [47], nano-antennas [43], micro-scale cavity [44], nano shaped resonator/granting [35] and convex groove [48].

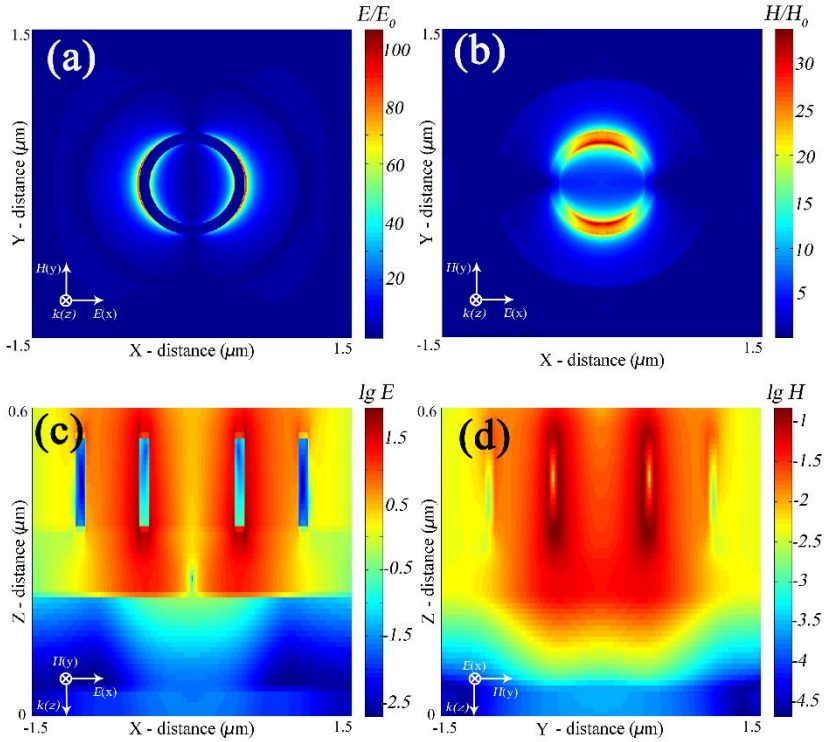

Fig. 5 Maps of electric and magnetic fields at resonant mode (M1) corresponding to **Fig. 4 d** (black line). **a** Enhancement factor, $\boldsymbol{E/E_0}$ in the x-y plane at z = 5 nm. **b** Enhancement factor, $\boldsymbol{H/H_0}$ in the x-y plane at z = 5 nm. **c** Spatial map of logarithmic electric intensity. **d** Spatial map of logarithmic magnetic intensity

Fig. 5c and d (also in Fig. 6) show the logarithmic electric and magnetic field intensity. It mirrors the energy field distribution around the rings. For the M1 resonance, electric and magnetic field are squeezed in the inner ring and the gap between two rings. Unlike the M1 resonance, the M2 resonance has slight distinction. Electric and magnetic field are confined in the gap between two rings while opened on the outside of the external ring for M2. This explained that the M2 peak (0.929 or -0.32 dB) is slightly

weaker than M1 (0.973 or -0.12 dB) because of the out-coupling of M2. At M1 resonance, most of the energy is focused in the inner ring. Therefore, the FWHM of M1 is sharper than M2. The ***E*** and ***H*** distribution reveal that the energy of the incidence is almost absorbed by the rings structure as illustrated by the marked color map.

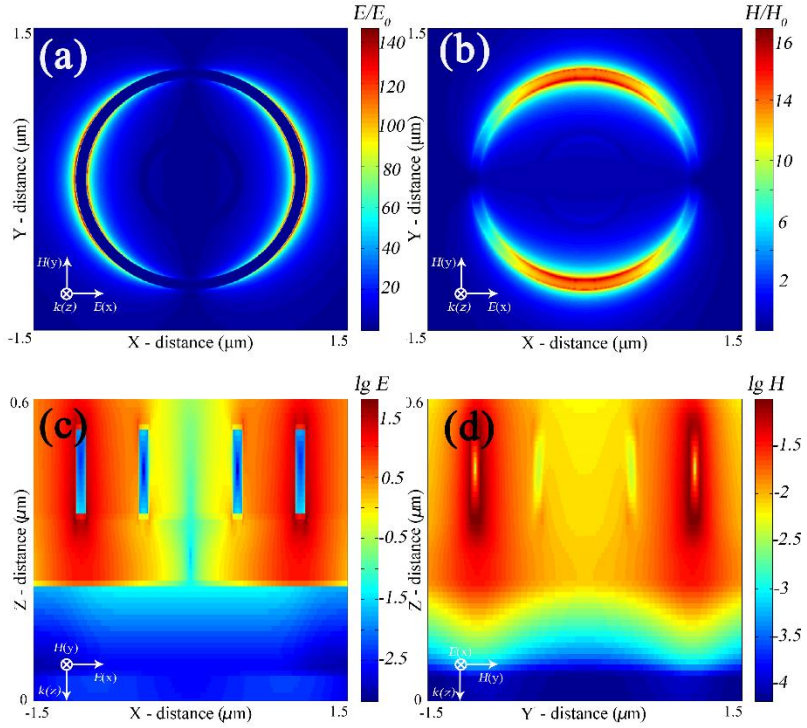

Fig. 6 Maps of electric and magnetic fields at resonant mode (M2) corresponding to **Fig. 4 d** (black line). **a** Enhancement factor, ***E/E₀*** in the x-y plane at z = 5 nm. **b** Enhancement factor, ***H/H₀*** in the x-y plane at z = 5 nm. **c** Spatial map of logarithmic electric intensity. **d** Spatial map of logarithmic magnetic intensity

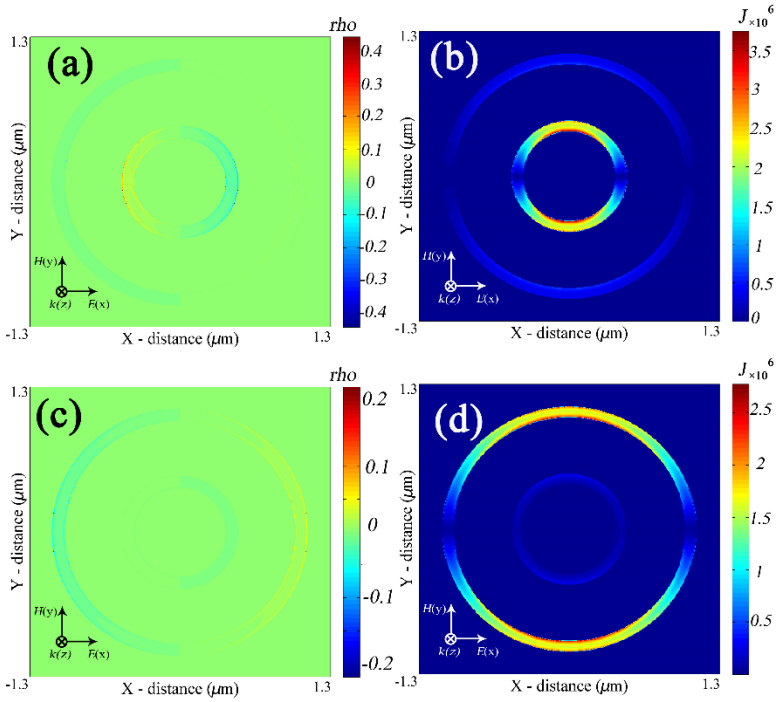

Fig. 7 Charge density and current density distribution of *x*-*y* plane at z = 100 nm depths at two resonant modes corresponding to **Fig. 4 d** (black line). **a**, **b** for M1. **c**, **d** for M2

For the M1 mode the current flow is confined almost entirely in the inner ring and region under ring, while the M2 mode is mainly associated with the external ring, as shown in Fig. 7b and d. The current underneath the excited ring (not shown in figure) is caused by image charge, which forms the loops and further triggers magnetic response. This means that two absorption peaks are caused by ohmic loss and dielectric loss. Such phenomenon is observed in fishnet-shaped [49], cross-shaped [43] and H-shaped [15] structure. Fig. 7a and c illustrate the charge density of x-y plane at z = 100 nm. They are agree with the near-field enhancement as plotted in Fig. 5 and Fig. 6 with strong charge buildup at two sides of the ring, confined to the edge of the metal. The current flow in ring and gold film is generated by magnetic response while the leakage current in spacer is caused by electric field. Thus electric and magnetic response depicts the perfect absorption of majority of energy with x-polarized electric field and y-polarized magnetic field. This suggests that symmetrical ring couples the electromagnetic wave with no energy loss at resonant frequency by large near-field enhancement capacitance provide by the gap between two rings for electric filed component and anti-parallel current flow for magnetic field component.

Though other resonators, such as patches, discs, demonstrate high absorptivity with polarization-nearly insensitive performance, they lack of scalability. In some cases, most of the possible light containing arbitrarily polarized components needs to be absorbed. The proposed split-ring resonator is completely polarization-independent because of its symmetry. Additionally, in our structure, adding an extra ring to achieve three absorption peaks are plotted in Fig. 8 a. Three peaks are distributed in MIR and FIR region, slightly influenced with each other. Therefore, it is flexible with tunable absorption peaks via controlling the number of the rings.

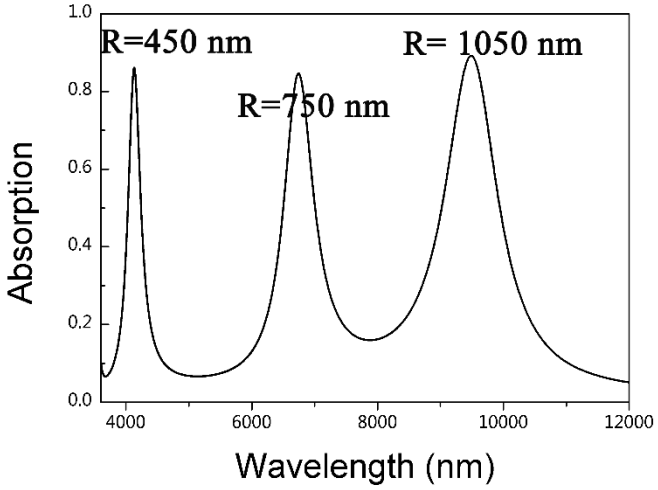

Fig. 8 Absorption spectra of the triple-band absorber

4. Conclusion

Overall, the MMPA structure incorporating the nano-rings achieves high absorptivity at targeted frequencies greater than 90% or -0.46 dB for a plane wave and is polarization-insensitive. Numerical full-wavelength FDTD simulations reveals that incident light is strongly absorbed within the two

resonant bands. The plasmonic nano-ring provides a large near-field enhancement which is 20~140 times larger than the non-plasmonic case. The work exhibits a significant progress toward achieving high-efficiency MMPAs that suppress the reflection at multiple bands within MIR and FIR region, though with trade-off between FWHM and desired wavelength. Our calculations show that the double-ring MMPA design is promising for MIR and FIR applications and exhibits excellent tunability over a broad spectral region, especially for multi-color photodetectors.

Acknowledgments

Authors appreciate the financial supports by the National Program on Key Basic Research Project (973 Program) No. 2013CB933301, National Program on Key Basic Research Project (973 Program) No. 2015CB358600.

References

1. Smith DR, Padilla WJ, Vier DC, Nemat-Nasser SC, Schultz S (2000) Composite medium with simultaneously negative permeability and permittivity. Physical Review Letters 84 (18):4184-4187. doi:10.1103/PhysRevLett.84.4184

2. Pendry JB (2000) Negative refraction makes a perfect lens. Physical Review Letters 85 (18):3966-3969. doi:10.1103/PhysRevLett.85.3966

3. Valentine J, Li JS, Zentgraf T, Bartal G, Zhang X (2009) An optical cloak made of dielectrics. Nature Materials 8 (7):568-571. doi:10.1038/nmat2461

4. Schurig D, Mock JJ, Justice BJ, Cummer SA, Pendry JB, Starr AF, Smith DR (2006) Metamaterial electromagnetic cloak at microwave frequencies. Science 314 (5801):977-980. doi:10.1126/science.1133628

5. Kurter C, Abrahams J, Anlage SM (2010) Miniaturized superconducting metamaterials for radio frequencies. Applied Physics Letters 96 (25):3. doi:10.1063/1.3456524

6. Kante B, Ourir A, Burokur SN, Gadot F, de Lustrac A (2008) Metamaterials for optical and radio communications. Comptes Rendus Physique 9 (1):31-40. doi:10.1016/j.crhy.2007.10.004

7. Edwards B, Alu A, Young ME, Silveirinha M, Engheta N (2008) Experimental verification of epsilon-near-zero metamaterial coupling and energy squeezing using a microwave waveguide. Physical Review Letters 100 (3):4. doi:10.1103/PhysRevLett.100.033903

8. Shelby RA, Smith DR, Nemat-Nasser SC, Schultz S (2001) Microwave transmission through a two-dimensional, isotropic, left-handed metamaterial. Applied Physics Letters 78 (4):489-491. doi:10.1063/1.1343489

9. Paulish AG, Zagubisalo PS, Kuznetsov SA, Ieee (2013) High-Performance Metamaterial MM-to-IR Converter for MM-wave Imaging. 2013 38th International Conference on Infrared, Millimeter, and Terahertz Waves (Irmmw-Thz)

10. Sajin G, Mocanu IA, Craciunoiu F (2013) MM-Wave Metamaterial Adjustable Antenna on Magnetically Biased Ferritic Substrate. International Journal of Antennas and Propagation. doi:10.1155/2013/696483

11. Zagubisalo PS, Paulish AG, Kuznetsov SA (2014) Simulation of Thermal Processes in Metamaterial MM-to-IR Converter for MM-wave Imager. 2nd International Conference on Mathematical Modeling in Physical Sciences 2013 (Ic-Msquare 2013) 490. doi:10.1088/1742-6596/490/1/012174

12. Neu J, Krolla B, Paul O, Reinhard B, Beigang R, Rahm M (2010) Metamaterial-based gradient index lens with strong focusing in the THz frequency range. Optics Express 18 (26):27748-27757. doi:10.1364/oe.18.027748

13. Scalari G, Maissen C, Turcinkova D, Hagenmueller D, De Liberato S, Ciuti C, Reichl C, Schuh D, Wegscheider W, Beck M, Faist J (2012) Ultrastrong Coupling of the Cyclotron Transition of a 2D Electron Gas to a THz Metamaterial. Science 335 (6074):1323-1326. doi:10.1126/science.1216022

14. Zolotovskii IO, Korobko DA, Minvaliev RN, Ostatochnikov VA (2014) A generator of far-infrared and terahertz radiation in nonlinear metamaterials exhibiting negative index of refraction. Optics and Spectroscopy 117 (5):822-831. doi:10.1134/s0030400x14110253

15. Jiang ZH, Yun S, Toor F, Werner DH, Mayer TS (2011) Conformal Dual-Band Near-Perfectly Absorbing Mid-Infrared Metamaterial Coating. Acs Nano 5 (6):4641-4647. doi:10.1021/nn2004603

16. Korobkin D, Urzhumov YA, Neuner B, III, Zorman C, Zhang Z, Mayergoyz ID, Shvets G (2007) Mid-infrared metamaterial based on perforated SiC membrane: engineering optical response using surface phonon polaritons. Applied Physics a-Materials Science & Processing 88 (4):605-609. doi:10.1007/s00339-007-4084-8

17. Yu Z, Veronis G, Fan S, Brongersma ML (2006) Design of midinfrared photodetectors enhanced by surface plasmons on grating structures. Applied Physics Letters 89 (15):151116. doi:10.1063/1.2360896

18. Helgert C, Menzel C, Rockstuhl C, Pshenay-Severin E, Kley EB, Chipouline A, Tuennermann A, Lederer F, Pertsch T (2009) Polarization-independent negative-index metamaterial in the near infrared. Optics Letters 34 (5):704-706

19. Sersic I, Frimmer M, Verhagen E, Koenderink AF (2009) Electric and Magnetic Dipole Coupling in Near-Infrared Split-Ring Metamaterial Arrays. Physical Review Letters 103 (21). doi:10.1103/PhysRevLett.103.213902

20. Christ A, Martin OJF, Ekinci Y, Gippius NA, Tikhodeev SG (2008) Symmetry breaking in a plasmonic metamaterial at optical wavelength. Nano letters 8 (8):2171-2175. doi:10.1021/nl0805559

21. Salandrino A, Engheta N (2006) Far-field subdiffraction optical microscopy using metamaterial crystals: Theory and simulations. Physical Review B 74 (7). doi:10.1103/PhysRevB.74.075103

22. Landy NI, Sajuyigbe S, Mock JJ, Smith DR, Padilla WJ (2008) Perfect metamaterial absorber. Physical Review Letters 100 (20):4. doi:10.1103/PhysRevLett.100.207402

23. Venkatesh S, Shrekenhamer D, Xu W, Sonkusale S, Padilla W, Schurig D (2013) Interferometric direction finding with a metamaterial detector. Applied Physics Letters 103 (25). doi:10.1063/1.4851936

24. Benz A, Krall M, Schwarz S, Dietze D, Detz H, Andrews AM, Schrenk W, Strasser G, Unterrainer K (2014) Resonant metamaterial detectors based on THz quantum-cascade structures. Scientific Reports 4:10. doi:10.1038/srep04269

25. Wang H, Yang Y, Wang LP (2014) Switchable wavelength-selective and diffuse metamaterial absorber/emitter with a phase transition spacer layer. Applied Physics Letters 105 (7):5. doi:10.1063/1.4893616

26. Kuznetsov SA, Paulish AG, Gelfand AV, Lazorskiy PA, Fedorinin VN (2012) MATRIX STRUCTURE OF METAMATERIAL ABSORBERS FOR MULTISPECTRAL TERAHERTZ IMAGING. Prog Electromagn Res 122:93-103. doi:10.2528/pier11101401

27. Wang Y, Sun TY, Paudel T, Zhang Y, Ren ZF, Kempa K (2012) Metamaterial-Plasmonic Absorber Structure for High Efficiency Amorphous Silicon Solar Cells. Nano letters 12 (1):440-445. doi:10.1021/nl203763k

28. Phillips J (2002) Evaluation of the fundamental properties of quantum dot infrared detectors. Journal of Applied Physics 91 (7):4590-4594. doi:10.1063/1.1455130

29. Guo B, Yang LQ, Hu WJ, Li WL, Wang HJ (2015) Effect of nano-sized cerium zirconium oxide solid solution on far-infrared emission properties of tourmaline powders. Modern Physics Letters B 29 (30):11.

doi:10.1142/s0217984915501833
30. Xu GK, Liang JS, Wang LJ, Meng JP, Liang GC (2005) Effects on combustion of gasoline of rare earth composite materials for far infrared radiation. J Rare Earths 23:247-250
31. Mizeikis V, Seet KK, Juodkazis S, Misawa H (2004) Three-dimensional woodpile photonic crystal templates for the infrared spectral range. Optics Letters 29 (17):2061-2063. doi:10.1364/ol.29.002061
32. Grant J, Ma Y, Saha S, Lok LB, Khalid A, Cumming DRS (2011) Polarization insensitive terahertz metamaterial absorber. Optics Letters 36 (8):1524-1526
33. Tao H, Bingham CM, Pilon D, Fan K, Strikwerda AC, Shrekenhamer D, Padilla WJ, Zhang X, Averitt RD (2010) A dual band terahertz metamaterial absorber. Journal of Physics D-Applied Physics 43 (22). doi:10.1088/0022-3727/43/22/225102
34. Tao H, Bingham CM, Strikwerda AC, Pilon D, Shrekenhamer D, Landy NI, Fan K, Zhang X, Padilla WJ, Averitt RD (2008) Highly flexible wide angle of incidence terahertz metamaterial absorber: Design, fabrication, and characterization. Physical Review B 78 (24). doi:10.1103/PhysRevB.78.241103
35. Wen Q-Y, Zhang H-W, Xie Y-S, Yang Q-H, Liu Y-L (2009) Dual band terahertz metamaterial absorber: Design, fabrication, and characterization. Applied Physics Letters 95 (24). doi:10.1063/1.3276072
36. Grant J, Ma Y, Saha S, Khalid A, Cumming DRS (2011) Polarization insensitive, broadband terahertz metamaterial absorber. Optics Letters 36 (17):3476-3478
37. Cheng YZ, Nie Y, Gong RZ, Yang HL (2011) Multi-band metamaterial absorber using cave-cross resonator. European Physical Journal-Applied Physics 56 (3). doi:10.1051/epjap/2011110206
38. Dayal G, Ramakrishna SA (2013) Design of multi-band metamaterial perfect absorbers with stacked metal-dielectric disks. Journal of Optics 15 (5). doi:10.1088/2040-8978/15/5/055106
39. Huang L, Chen H (2011) MULTI-BAND AND POLARIZATION INSENSITIVE METAMATERIAL ABSORBER. Prog Electromagn Res 113:103-110. doi:10.2528/pier10122401
40. Ye Q, Liu Y, Lin H, Li M, Yang H (2012) Multi-band metamaterial absorber made of multi-gap SRRs structure. Applied Physics a-Materials Science & Processing 107 (1):155-160. doi:10.1007/s00339-012-6796-7
41. Zhang N, Zhou PH, Cheng DM, Weng XL, Xie JL, Deng LJ (2013) Dual-band absorption of mid-infrared metamaterial absorber based on distinct dielectric spacing layers. Optics Letters 38 (7):1125-1127
42. Shen X, Cui TJ, Zhao J, Ma HF, Jiang WX, Li H (2011) Polarization-independent wide-angle triple-band metamaterial absorber. Opt Express 19 (10):9401-9407. doi:10.1364/OE.19.009401
43. Chen K, Adato R, Altug H (2012) Dual-Band Perfect Absorber for Multispectral Plasmon-Enhanced Infrared Spectroscopy. Acs Nano 6 (9):7998-8006. doi:10.1021/nn3026468
44. Mao FL, Xie JJ, Xiao SY, Komiyama S, Lu W, Zhou L, An ZH (2013) Plasmonic light harvesting for multicolor infrared thermal detection. Optics Express 21 (1):295-304. doi:10.1364/oe.21.000295
45. Rakić AD, Djurišić AB, Elazar JM, Majewski ML (1998) Optical properties of metallic films for vertical-cavity optoelectronic devices. Applied Optics 37 (22):5271-5283. doi:10.1364/AO.37.005271
46. Palik ED (1985) Handbook of optical constants of solids. Academic Press, Orlando
47. Tang L, Miller DAB, Okyay AK, Matteo JA, Yuen Y, Saraswat KC, Hesselink L (2006) C-shaped nanoaperture-enhanced germanium photodetector. Optics Letters 31 (10):1519-1521. doi:10.1364/ol.31.001519
48. Beermann J, Eriksen RL, Sondergaard T, Holmgaard T, Pedersen K, Bozhevolnyi SI (2013) Plasmonic black metals by broadband light absorption in ultra-sharp convex grooves. New Journal of

Physics 15:16. doi:10.1088/1367-2630/15/7/073007
49. Kafesaki M, Tsiapa I, Katsarakis N, Koschny T, Soukoulis CM, Economou EN (2007) Left-handed metamaterials: The fishnet structure and its variations. Physical Review B 75 (23):235114